Biophysical Chemistry 253 (2019) 106225

Contents lists available at ScienceDirect

Biophysical Chemistry

journal homepage: www.elsevier.com/locate/biophyschem

Fluorescence imaging of biochemical relationship between ubiquitinated histone 2A and Polycomb complex protein BMI1

Barbara Storti[a,*], Simone Civita[a], Paolo Faraci[a], Giorgia Maroni[b,c,d], Indira Krishnan[b,c], Elena Levantini[b,c,d,e], Ranieri Bizzarri[a,f]

[a] NEST, Scuola Normale Superiore and Istituto Nanoscienze-CNR, Piazza San Silvestro 12, 56127 Pisa, Italy
[b] Beth Israel Deaconess Medical Center, 330 Brookline Ave, MA, Boston 02215, USA
[c] Harvard Medical School, 25 Shattuck St, MA, Boston 02115, USA
[d] Institute of Biomedical Technologies, National Research Council (CNR), Area della Ricerca di Pisa, via Moruzzi 1, 56124 Pisa, Italy
[e] Harvard Stem Cell Institute, 7 Divinity Ave, MA, Cambridge 02138, USA
[f] Department of Surgical, Medical and Molecular Pathology, and Critical Care Medicine, via Roma 67, Pisa 56126, Italy

HIGHLIGHTS

- Confocal microscopy highlights the BMI1-driven ubiquitination of H2A in NSCLC cells.
- The level of ubiquitinated H2A depends linearly on BMI1 expression.
- BMI1 dynamically assembles in cPRC1 to ubiquitinate Histone 2A.
- BMI1-containing cPRC1 has predominant role in the ubiquitination of H2A.

GRAPHICAL ABSTRACT

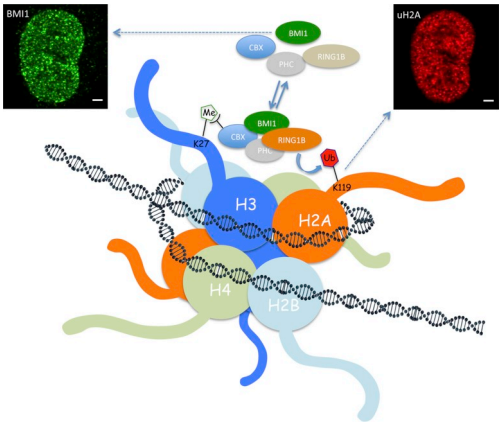

ARTICLE INFO

Keywords:
BMI1
Ubiquitinated H2A
Non-small cell lung Cancer (NSCLC)
A549
PTC-209
Indirect immunofluorescence
Confocal microscopy
Functional colocalization
Pearson's coefficient

ABSTRACT

Several *in vitro* experiments have highlighted that the Polycomb group protein BMI1 plays a pivotal role in determining the biological functions of the Polycomb Repressor Complex 1 (PRC1), including its E3-ligase activity towards the Lys^{119} of histone H2A to yield ubiquitinated uH2A. The role of BMI1 in the epigenetic activity of PRC1 is particularly relevant in several cancers, particularly Non-Small Cell Lung Cancer (NSCLC). In this study, using indirect immunofluorescence protocols implemented on a confocal microscopy apparatus, we investigated the relationship between BMI1 and uH2A at different resolutions, in cultured (A549) and clinical NSCLC tissues, at the single cell level. In both cases, we observed a linear dependence of uH2A concentration upon BMI1 expression at the single nucleus level, indicating that the association of BMI1 to PRC1, which is needed for E3-ligase activity, occurs linearly in the physiological BMI1 concentration range. Additionally, in the NSCLC cell line model, a minor pool of uH2A may exist in absence of concurrent BMI1 expression, indicating non-exclusive, although predominant, role of BMI1 in the amplification of the E3-ligase activity of PRC1. A pharmacological downregulator of BMI1, PTC-209, was also tested in this context. Finally, the absence of

* Corresponding author.
E-mail address: barbara.storti@nano.cnr.it (B. Storti).

https://doi.org/10.1016/j.bpc.2019.106225
Received 27 March 2019; Received in revised form 10 July 2019; Accepted 10 July 2019
Available online 11 July 2019

significant colocalization (as measured by the Pearson's coefficient) between BMI1 and uH2A submicron clusters hints to a dynamic model where PRC1 resides transiently at ubiquitination sites. Beside unveiling subtle functional relationships between BMI1 and uH2A, these results also validate the use of uH2A as downstream "reporter" for BMI1 activity at the nuclear level in NSCLC contexts.

1. Introduction

Histones function to compact DNA into nucleosomes, which are the basic unit of chromatin. Each nucleosome is composed of a segment of 146 bp of DNA wrapped around eight histone core proteins (two copies each of H2A, H2B, H3, and H4) which are sealed by the linker histone H1 [1]. Post-transcriptional modifications on histone tails, which are flexible structures that protrude from the nucleosome core, play crucial roles in cellular processes including transcription, replication, and DNA repair [2]. Unique among core histone proteins, H2A is mono-ubiquitinated at lysine 119 on the C-terminus stretch exposed to the nucleosomal surface [3]. Interestingly, monoubiquitinated H2A (uH2A) is rather abundant, as it accounts for 5–15% of total H2A levels [3]. At odds with polyubiquitination, which usually targets proteins for proteolytic destruction, formation of uH2A has been recently recognized as a relevant epigenetic strategy to control gene expression [4]. For example, uH2A was found to be essential for maintaining repression of target genes and to hamper cell differentiation [5,6].

Ubiquitin is conjugated to the target proteins through the concerted action of an ATP-dependent ubiquitin-activating enzyme (E1), an ubiquitin conjugating enzyme (E2), and an ubiquitin ligase (E3), which confers substrate specificity [7]. In most metazoan species, ubiquitination of H2A is mediated mainly by the Polycomb Repressive Complex 1 (PRC1), a multisubunit protein complex [8,9]. The canonical PRC1 (cPRC1) assembles around four core proteins: CBX (*polycomb protein*; CBX2/4/6/7/8), PCGF (*polycomb group zinc fingers*; PCGF2/4), PHC (*polyhomeotic homologues*; PHC1/2/3), and RING (RING1A/B) [8,10]. Other four PCGF proteins (PCGF1, PCGF3, PCGF5, and PCGF6) assemble around RING1A/B and RYBP/YAF2 proteins to yield the so-called variant PRC1 complexes [8]. This variant is believed to provide unique targeting modalities and regulatory capacity to PRC1.

In particular the site of cPRC1 activity is signaled by the presence of trimethylated histone H3 at lysine 27, which is recognized and bound by the chromobox protein CBX [9]. The E3 ligase activity of cPRC1 is conferred by the heterodimer of RING1A/B with PCGF2/4 [11]. PCGF4, better known as BMI1 (B cell-specific Moloney murine leukemia virus integration site 1) was shown to be a key regulatory component of cPRC1, since it establishes protein-protein interactions that stabilize the overall architecture of the complex [12]. BMI1 itself has no E3-ligase activity but it promotes a more favorable interaction of the BMI1-RING1A/B heterodimer with nucleosome substrates, which results in an efficient site-specific monoubiquitination [11]. Notably, BMI1 is an important crosspoint in at least 16 different types of cancer and stands out as a promising target within the small list of genes known to regulate the function of cancer cells [12]. The epigenetic role of BMI1 expression in Non-Small Cell Lung Cancer (NSCLC) is particularly intriguing since BMI1 overexpression drives stem-like properties associated with induction of epithelial-mesenchymal transition (EMT) that promotes invasion and metastasis resulting in a poor prognosis for the patient [13]. Additionally, we have recently shown a clear prognostic relationship between lower patient survival and BMI1 overexpression in a large cohort of NSCLC patients characterized by concomitant low C/EBPα and high BMI1 expression [14]. This pattern can be reversed in *in vivo* animal models of lung cancer by compounds targeting selectively BMI1 [14], such as PTC-209 which downregulates Bmi1 [15]. Indeed, accumulating evidence has revealed that BMI1 represents a promising therapeutic target with considerable translational potentials [16]. The pivotal oncogenic role of BMI1 is most likely related to its chromatin remodeling properties, and the E3-ligase activity of cPRC1 is probably the most representative example.

To the best of our knowledge, however, the biochemical relationship between BMI1 and uH2A has never been investigated at the cellular level,. Single cell measurements of biochemical processes are increasingly recognized as quintessential to the full understanding of biological mechanisms [17], as they afford spatial and temporal features that are accessible by classical *ex-vivo* biochemical methods. In the present case, we set out to analyze the quantitative correlation between BMI1 and uH2A at nuclear and sub-nuclear spatial scales, as a way to investigate the dependence of E3-ligase activity of cPRC1 on BMI1 amount, in endogenous conditions in lung cancer cells, as well as under pharmacological inhibition, and to validate uH2A as reporter of BMI1 concentration at the single cell level.

Our single cell quantification at both nuclear and sub-nuclear scales exploited the exquisite sensitivity of confocal fluorescence microscopy [18–20]. To avoid perturbation of the endogenous protein concentrations, we targeted intracellular BMI1 and uH2A by indirect immunofluorescence (IIF). Immunofluorescence (IF) is a cell imaging technique that relies on the use of antibodies to label a specific target antigen with a fluorophore. The antibody that is directed towards the target antigen is called *primary* antibody, and in direct IF it is conjugated with a fluorophore. In IIF the primary antibody is unconjugated and becomes the target of a *secondary*, fluorescently labeled, antibody. The advantage of IIF is the increased achievable sensitivity obtained through signal amplification from multiple secondary antibodies binding to a single primary antibody.

Through our approach we were able to visualize, at different spatial scales, the quantitative relationship between BMI1 and uH2A in cultured A549 cells. A549 cells carry a *K-Ras*^{G12D} mutation, frequently found in NSCLC patients [21], and were demonstrated to represent a useful cellular model for investigating the role of BMI1 in NSCLC [14]. Our confocal IIF results obtained on A549 cells quantitatively highlight the strong correlation between BMI1 and uH2A amounts in the whole nucleus in naïve conditions, as well as under pharmacological inhibition of BMI1. Conversely, uH2A and BMI1 are less correlated at the submicron resolution scale of the confocal microscope (240–270 nm), most likely given the highly dynamic E3 ligase activity of cPRC1. Remarkably, statistically significant uH2A *vs.* BMI1 correlation was demonstrated also in the nuclei of NSCLC tissue cells, with distinguishable trends between neoplastic epithelial cells and neighboring stromal areas.

2. Materials and methods

Chemicals (with the exception of antibodies, see below) and solvents were purchased from Sigma-Aldrich Italy (Milan, Italy).

2.1. Primary antibodies

- 8240S Rabbit anti-human Ubiquityl-Histone H2A monoclonal antibody (herein referred to as r-huH2A) was purchased from Cell Signaling Technologies (EuroClone, Milan, Italy).
- sc-390443 Mouse anti-human BMI1 monoclonal antibody (herein referred to as m-hBMI1) was purchased from Santa Cruz Biotechnology (Dallas TX, USA).
- sc-101540 Rat anti-Karyopherin α1/6 monoclonal antibody (herein referred to as R-hImpα) was purchased from Santa Cruz Biotechnology (Dallas TX, USA).

2.2. Secondary antibodies

- A32723 Goat anti-mouse IgG AlexaFluor 488 (herein referred to as m-488) was purchased from Life Technologies Italy (Monza, Italy).
- A11006 Goat anti-Rat IgG AlexaFluor 488 (herein referred to as R-488) was purchased from Life Technologies Italy (Monza, Italy).
- A31573 Donkey anti-rabbit IgG AlexaFluor 647 (herein referred to as r-647c) was purchased from Life Technologies Italy (Monza, Italy).
- 711-605-151 Donkey anti-mouse IgG Cy3 (herein referred to as m-Cy3) was purchased from Jackson ImmunoResearch (Li-Starfish S.r.l, Cernusco sul Naviglio, Italy).
- 711-605-152 Donkey anti-Rabbit IgG AlexaFluor 647 (herein referred to as r-647t) was purchased from Jackson ImmunoResearch (Li-Starfish S.r.l, Cernusco sul Naviglio, Italy).

2.3. Cell culture

Adenocarcinoma human alveolar basal epithelial cells (A549) were grown in Roswell Park Memorial Institute (RPMI) 1640 medium (RPMI 1640, Invitrogen, Carlsbad, CA) supplemented with 10% Fetal Bovine Serum (FBS), glutamine (2 mM), 100 U/ml penicillin and 100 mg/ml streptomycin (Invitrogen). Cells were maintained at 37 °C in a humidified 5% CO_2 atmosphere. For live imaging, 6-7 × 10^4 cells were plated on a 35-mm glass bottom dish (Willco-dish HBST-3512/1.5-0.005) 24–48 h before performing the immunofluorescence experiments.

2.4. Drug treatment

The BMI1 modulator molecule (PTC-209) was provided by PTC Therapeutics. PTC-209 in DMSO was added at a concentration of 1.5 μM for 48 h to A549 cells, plated into Willco-dish, before performing the immunofluorescence experiments. Control cells were exposed to 0.5% DMSO for the same amount of time.

2.5. Cell indirect immunofluorescence protocol

A549 cells were washed with phosphate buffer saline 1× (PBS, 3 times) and then fixed with paraformaldehyde (2% in PBS) for 15 min. After washing with PBS (3 times), cells were permeabilized with 0.1% Triton X-100 (in PBS) for 15 min. Cells were then washed with PBS (3 times), 0.5% Bovine Serum Albumin in PBS (PBB, 4 times), and exposed for 40 min to 2% Bovine Serum Albumin in PBS (BSA 2%). After washing with PBB (4 times), cells were incubated with the primary antibody diluted in PBB (for concentrations see below) for 1 h at room temperature (RT) and 1.5 more hour at 4 °C. Cells were washed with PBB (4 times), and incubated with the secondary antibody diluted in PBB (for concentrations see below) for 1 h at RT in the dark. Next, cells were washed with PBB (4 times), stained with Hoechst 33342 (1 mg/100 ml in water) for 30 s, and washed with PBS (three times). Cells were maintained in PBS at 4 °C before imaging no longer than 7 days.

Negative controls were obtained by the same procedure, but incubating cells with PBB only, instead of a primary antibody solution in PBB.

2.6. Tissue immunofluorescence protocol

Paraffin-embedded tissues were sectioned at 5 μm thickness. Tissue sections were deparaffinized with Xylene and hydrated in graded ethanol. Antigen retrieval was performed in a pressure cooker for 10 min in 10 mM citrate buffer pH 6.0. Protein blocking with 5% donkey serum in PBS was applied for 30 min at RT. The sections were incubated with the primary antibody at 4C° overnight. After washing with PBS, sections were incubated with the secondary antibody for one hour at RT. After washing, tissue sections were mounted with Prolong Gold anti-fade mounting medium.

2.6.1. Antibody dilutions from mother (commercial) solutions

		IF on cells	IF on tissue
Primary antibodies	m-hBMI1	3/500 [1.2 μg/ml] (in PBB)	1/200 [1 μg/ml] (in PBS)
	R-hImpα	3/500 [1.2 μg/ml] (in PBB)	
	r-huH2A	1/1600[a] (in PBB)	1/750[a] (in PBS)
Secondary antibodies	m-488	1/200 [10 μg/ml] (in PBB)	
	R-488	1/250 [8 μg/ml] (in PBB)	
	m-Cy3		1/300 [5 μg/ml] (in PBS)
	r-647c	1/250 [8 μg/ml] (in PBB)	
	r-647t		1/300 [1 μg/ml] (in PBS)

[a] Concentration was not provided by the manufacturer.

2.7. Confocal fluorescence microscopy

Fluorescence was measured by a confocal Zeiss LSM 880 with Airyscan (Carl Zeiss, Jena, Germany), supplied with GaAsP detectors (Gallium:Arsenide:Phosphide). Samples were viewed with a 63× Apochromat NA = 1.4 oil-immersion objective. We adopted 0.9× zoom for imaging multiple cells and tissues (1 pixel = 220 nm), and 4-6× zoom to image single A549 nuclei (1 pixel = 30–50 nm).

The pinhole size was set to 44 μm, which corresponds to 1 airy unit (AU) for the green acquisition channel. Pixel dwell time was adjusted to 1.52 μs and 512 × 512 pixel images were collected.

Each line of the image was acquired in three channels sequentially (line mode), and each line was averaged four times to improve sensitivity. Cells were imaged at the focal depth that maximizes the nuclear section on the image plane.

The acquisition channels were set as follows:

2.8. Single cell image analysis on A549 cells

	Acquisition channel			
	Blue (Hoechst 33342)	Green (Alexa488)	Red (Cy3)	Far-Red (Alexa647)
A549 cells	λ_{ex} = 405 λ_{em} = 420–500 nm	λ_{ex} = 488 λ_{em} = 500–560 nm	–	λ_{ex} = 640 λ_{em} = 650–700 nm
Tissue	λ_{ex} = 405 λ_{em} = 420–500 nm	–	λ_{ex} = 561 λ_{em} = 570–610 nm	λ_{ex} = 640 λ_{em} = 650–700 nm

512 × 512 pixel confocal images (Hoechst, Green, and Far-red channels) were analyzed using ImageJ (NIH), version 1.52e by a custom-made macro (available upon request) that involved:

a. Gaussian blur of the blue channel image (sigma: 1 pixel).
b. Background subtraction in the blue channel image (rolling ball radius: 1000 pixels).
c. Thresholding (Method: Huang [22]).
d. Filling holes and watershed separation of the thresholded image.
e. Particle analysis upon the 3 channels using the thresholded image as mask (command: particle analysis).
f. Detection of internuclear separation by the *Nearest Neighbor Distances Calculations* plugin (https://icme.hpc.msstate.edu/

mediawiki/index.php/Nearest_Neighbor_Distances_Calculation_with_ImageJ)

For each nucleus in the image, the analysis yielded the mean Hoechst, Alexa488, and Alexa647 fluorescence per pixel (F_H, F_{488}, F_{647}), and other morphological parameters of the cell nucleus such as the area (A_N), perimeter (P_N), and circularity (C, calculated as $C = 4\pi \cdot A_N/P_N^2$). Then, we calculated the mean Alexa488 and Alexa647 fluorescence per nucleus of the negative control sample ($\overline{F}^0_{488}, \overline{F}^0_{647}$).

To provide the calibration factor between secondary antibody concentration and fluorescence (g_{488}, g_{647}), we imaged the incubation solution of the secondary antibody with the same confocal setup as cells. To maximize the similarity between calibration solution and cells, the incubation solution was added to PFA-fixed A549 pre-stained with Hoechst and images of the extracellular space filled with the antibody solution were taken at the same focal depth at which immunostained cells were imaged.

Finally, for each cell the concentration of BMI1 and uH2A was obtained by:

$$[BMI1] = \frac{(F_{488} - \overline{F}^0_{488})}{g_{488}}; [uH2A] = \frac{(F_{647} - \overline{F}^0_{647})}{g_{647}}$$

Impα concentration was obtained as for BMI1, and also in this case the green channel was utilized. In all instances, the concentration units were in μM and we assumed 150,000 D as the molecular weight of the secondary antibody.

We should note that the above equations assume a 1:1 ratio between each target protein and the secondary antibody, in absence of any reliable information on the stoichiometry of antigen-primary-secondary recognition complex.

2.9. Single cell image analysis on cells within tissues

512 × 512 pixel confocal images (Hoechst, Orange, and Far-red channels) of immunostained tissues were analyzed as previously described for the A549 cell line. The only difference was represented *by the absence* of the concentration quantification step, because of the large optical difference between the calibration solution containing the secondary antibodies and the tissue itself.

Thus, the amounts of BMI1 and uH2A were expressed as fluorescence counts and calculated according to:

$$[BMI1] = (F_{561} - \overline{F}^0_{561}); [uH2Au] = (F_{647} - \overline{F}^0_{647})$$

2.10. Determination of the confocal resolution on the object plane

The resolution of the confocal microscope on the object (xy) plane (d_{xy}) was determined by the Fourier Ring Correlation (FRC) Method [23]. In short, due to diffraction, a microscope behaves as a short-pass filter with a fixed cutoff frequency: the sample's frequencies beyond the diffraction limit are not transmitted to the image, and this identifies the maximum resolution of the system. The FRC measures the degree of correlation of the two images at different spatial frequencies: at spatial frequencies below the cutoff, the two images are strongly correlated, but at spatial frequencies above the cutoff, non- correlated noise realizations dominate. Thus, we may retrieve the effective cutoff as the frequency at which the correlation curve drops below a given threshold. The two independent images can be obtained by registering two sequential frames at high zoom, in order to minimize the pixel dimension and adequately sample spatial frequencies well below the cutoff. Accordingly, two IIF confocal images were sequentially taken on a set of A549 cells at zoom 4 × – 6 × (pixel size around 30–50 nm) and each set of two sequential images were analyzed by the *Fourier Ring Correlation* plugin (https://imagej.net/Fourier_Ring_Correlation_Plugin) of ImageJ or Fiji (NIH, Bethesda USA), setting the frequency threshold to 1/7 [23]. We found $d_{xy} = 241 \pm 4$ nm for the green acquisition channel and $d_{xy} = 274 \pm 7$ nm for the far-red acquisition channel. The blue acquisition channel was not analyzed, as we were not interested in DNA measurements at confocal resolution. Note that the theoretical resolutions for the green and far-red acquisition channels, as determined by the Abbe's criterion from the Numeric Aperture of the objective and the average emission wavelength [24], are $d_{xy} = 189$ nm (green) and $d_{xy} = 241$ nm (far-red), respectively.

2.11. Colocalization analysis on A549 cells

Colocalization of the green and far-red images of A549 nuclei acquired at high zoom (4 × –6 ×) was quantified by the Pearson's coefficient *R* after thresholding and significance test, according to the method by Costes et al. [25]. Analysis was carried out by the *colocalization threshold* and *colocalization test* routines of Fiji (NIH, Bethesda, USA).

2.12. Statistical data analysis

Statistical analyses and data fitting were carried out by the GraphPad Prism 7 package (GraphPad Software, San Diego CA, USA). Linear fitting was carried out by weighting data by $1/Y^2$, where Y is the dependent variable (in our case: [uH2A] or fluorescence of uH2A).

3. Results

3.1. Indirect immunofluorescence on A549 cells

IIF can multiplex detection of different targets by selecting primary antibodies belonging to orthogonal species, and secondary antibodies specific for those species. In our experiments, we targeted human BMI1 with a mouse primary IgG, whereas human uH2A was recognized by a rabbit primary IgG.

To maximize the sensitivity of our IIF analysis, we minimized fluorescent cross-talk between the two markers to a negligible extent, by selecting secondary antibodies labeled by fluorophores emitting into two well-separated spectral regions (Green acquisition channel: Alexa488, antibody: m-488; far-red acquisition channel: Alexa647, antibody r-647c). Note that m-488 targeted the mouse primary antibody against BMI1; and r-647 targeted the rabbit primary antibody against uH2A. DNA was stained with a third blue emitter (Blue acquisition channel: Hoechst 33342). This colour combination allowed for a line-by-line concomitant generation of a confocal image for each acquisition channel. By a segmentation algorithm based on DNA staining, nuclei were identified and the fluorescence of each acquisition channel was measured in each pixel.

Upon calibration (see Materials and Methods), the emissions collected in the green and far-red acquisition channels were converted into the concentrations of m-488 and r-647c, respectively. We assumed a fixed 1:1 stoichiometric ratio between secondary antibody and antigen, *i.e.* we identified the concentrations of BMI1 and uH2A with those of m-488 and r-647c, respectively. Different stoichiometric ratios are indeed possible, on account of the signal amplification of IIF. Yet, the generality of our treatment remained unaffected, since we were interested in the *correlations* among protein concentrations rather than in their absolute values.

3.2. Single-cell analysis of BMI1-uH2A correlation in A549 cells

Five different biological replicates of A549 cell line ($n = 732$ cells overall) were maintained in proper culture medium conditions and subjected to IIF for BMI1 and uH2A, by detecting the fluorescence through a confocal microscope. In all cells, the fluorescence of BMI1 and uH2A was observed mostly at the nuclear level (Fig. 1), in agreement with previous IIF studies [6,26]. For each cell, the nuclear concentrations of both proteins were measured and reported in the uH2A

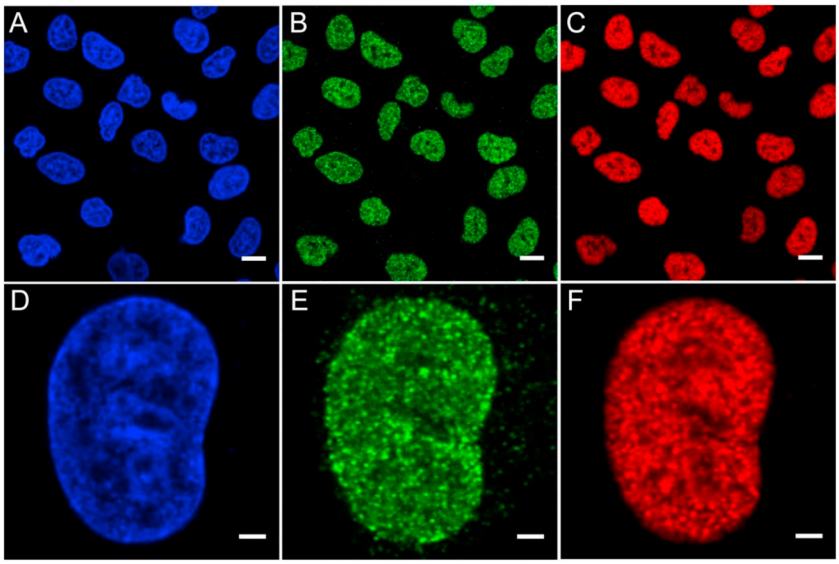

Fig. 1. Fluorescence nuclear imaging of DNA, BMI1 and uH2A in A549 cell line by confocal microscopy. (A, D) DNA staining by Hoechst 33342 (Blue acquisition channel). (B, E) BMI1 staining by immunofluorescence; secondary antibody (m-488) was labeled with Alexa488 (green acquisition channel). (C, F) uH2A staining by immunofluorescence; secondary antibody (r-647c) labeled with Alexa647 (far-red acquisition channel). Scale bar for A, B, C: 10 μm. Scale bar for D, E, F: 2 μm. (For interpretation of the references to colour in this figure legend, the reader is referred to the web version of this article.)

vs. BMI1 cell plot (Fig. 2). Qualitatively, the monotonous positive trend of uH2A with increasing BMI1 expression highlighted the strong correlation between the two proteins. This relationship was quantitatively demonstrated by the high-value of the Spearman non-parametric correlation test ($r = 0.725$, $p < .0001$).

Inspection of the uH2A *vs.* BMI1 plot afforded further information. For low to null BMI1 concentration, a minimal residual uH2A pool was present. Yet, for high BMI1 concentrations, uH2A increased more than ten-fold with respect to this initial pool (Fig. 2). Data fitting analysis indicated that a linear model could account for the observed uH2A *vs.* BMI1 trend (Fig. 2, $\chi^2 = 0.889$). More complicated biochemical reaction schemes, such as Hill cooperative model, did not improve the chi-square fitting and were not considered (data not shown).

The strong physiological correlation between BMI1 and uH2A was further validated by replacing BMI1 with Importin-α (Impα) in IIF on A549 ($n = 300$ cells in total). Impα is not involved in the E3-ligase activity of cPRC1, albeit its localization is predominantly nuclear (Fig. 3). Plot of uH2A *vs.* Impα indeed clearly showed the weak correlation between the two proteins (Fig. 4), which was confirmed by the Spearman non-parametric correlation test ($r = 0.394$, $p < .0001$), strengthening confidence in our approach.

Of note, BMI1 and uH2A concentrations showed a weak correlation with both nuclear area and circularity ($r < 0.2$, $p < .0001$). A similar weak correlation between nuclear area and BMI1 concentration was recently described for HEK cells [27]. Finally, no correlation ($0 < r < 0.1$, $p > .1$) was found between BMI1 (or uH2A) and the average internuclear distance, suggesting that in our samples cell density (confluence: 60–70%) had a negligible role on BMI1 (and uH2A) expression levels.

3.3. Single-cell analysis of BMI1-uH2A correlation in A549 cells under PTC-209 treatment

Three different replicates of A549 cells ($n = 508$ cells) were exposed for 48 h to PTC-209, following the procedure reported in [14]. Additional cells ($n = 770$ cells) were treated with DMSO as a control. Upon PTC-209 treatment, dramatic changes in cell morphologies could be detected. More specifically, a large fraction (> 70%) of round-shaped non-adhering cells was visible (Fig. 5). This fraction is most likely associated to the large percentage of cells arrested in non-dividing state (G_0), as we have previously demonstrated upon PTC-209 treatment [14].

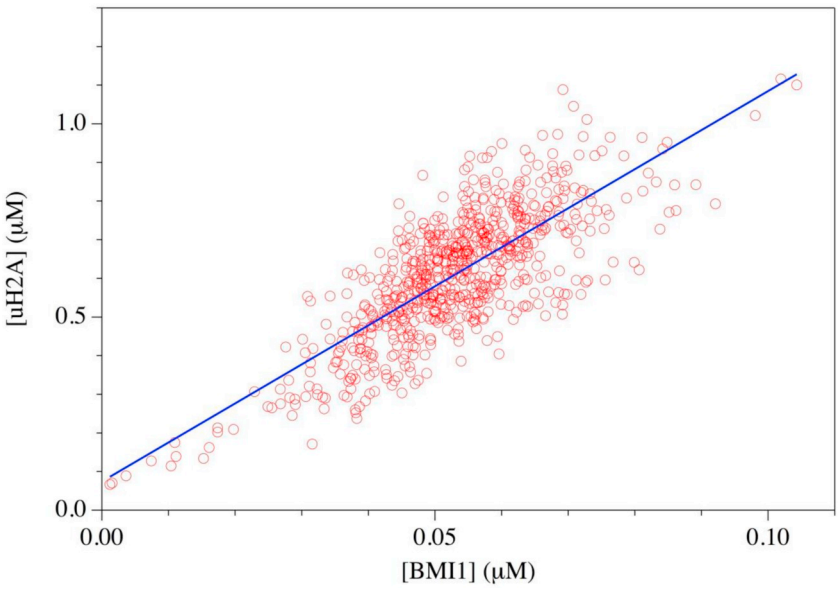

Fig. 2. uH2A *vs.* BMI1 cell plot from A549 cells. The fluorescence associated to the immunorecognition of nuclear BMI1 and uH2A is converted to protein concentrations (see Materials and Methods) and plotted. Each red open circle represents a single nucleus. The blue line is the linear fitting of the dataset. (For interpretation of the references to colour in this figure legend, the reader is referred to the web version of this article.)

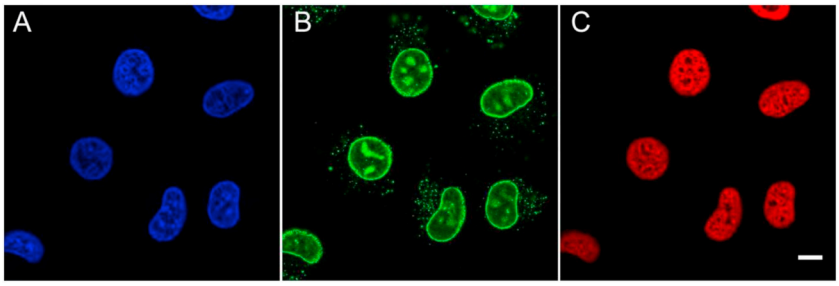

Fig. 3. Fluorescence nuclear imaging of DNA, Impα and uH2A in A549 cell line by confocal microscopy. (A) DNA staining by Hoechst 33342 (Blue acquisition channel). (B) Impα staining by immunofluorescence; secondary antibody (R-488) labeled with Alexa488 (green acquisition channel). (C) uH2A staining by immunofluorescence; secondary antibody (r-647c) labeled with Alexa647 (far-red acquisition channel). Scale bar: 10 μm. (For interpretation of the references to colour in this figure legend, the reader is referred to the web version of this article.)

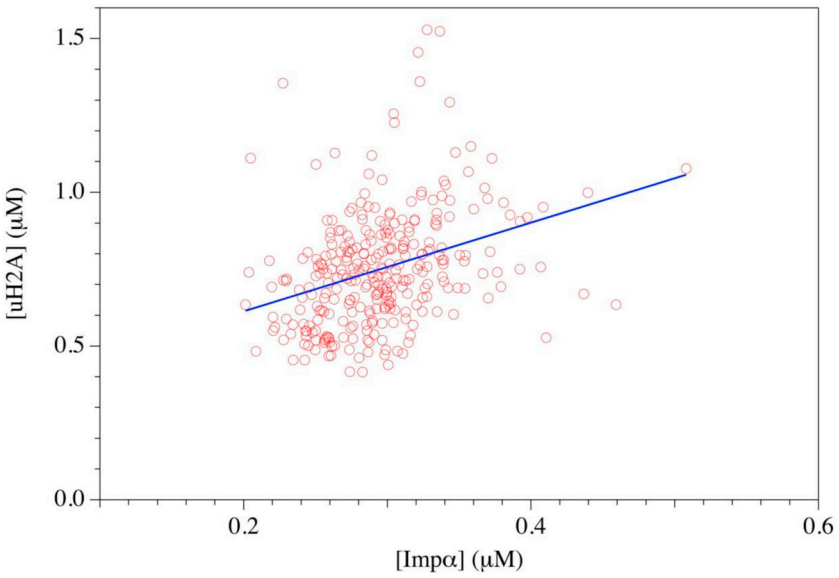

Fig. 4. uH2A *vs.* Impα cell plot from A549 cells. The fluorescence associated to the immunorecognition of nuclear Impα and uH2A is converted to protein concentrations (see Materials and Methods) and plotted. Each red open circle represents a single cell. The blue line is the linear fitting of the dataset. (For interpretation of the references to colour in this figure legend, the reader is referred to the web version of this article.)

As expected, PTC-209-treated cells showed an overall decrease of BMI1 expression, however different degrees of BMI1 downregulation have been observed. In particular, in the round-shaped non-adhering cells, representing the largest fraction, BMI1 expression was nearly abolished (Fig. 6, row C and F), whereas it was decreased by 49% in the remaining adhering cells (Fig. 6, row B and E), as compared to vehicle treated cells (Fig. 6, row A and D) taken as 100% reference. Remarkably, the emission of uH2A showed a similar pattern as BMI1 in both fractions (round-shaped non-adhering and adhering) upon PTC-209 treatment, as compared to control cells: uH2A was negligible in the round-shaped not-adhering cells (Fig. 6, row C and F), and adhering cells displayed on average 70% loss of uH2A (Fig. 6, row B and E). All these findings are in excellent agreement with the strong downregulation of BMI1 by [14] and its downstream effector uH2A [28]. It is worth noting that many non-adhering cells detached upon the IIF procedure, reducing the pool of round cells to < 20% in our fluorescence images.

Overall, our data indicate that the strong correlation between BMI1 and uH2A concentrations is well maintained even after pharmacological downregulation of BMI1 ($r = 0.735$, $p < .0001$) in all cells characterized by non-negligible BMI1 and uH2A concentrations (thus, mostly adhering cells). The biochemical relationship between the two biomarkers is clearly demonstrated also in the single cell plot of uH2A *vs.* BMI1 concentrations (Fig. 7). Unlike untreated cells, however, this relationship is not univocal: ~ 40% of the drug-treated cells with non-negligible BMI1 and uH2A, fit the linear trend of control cells (Fig. 7,

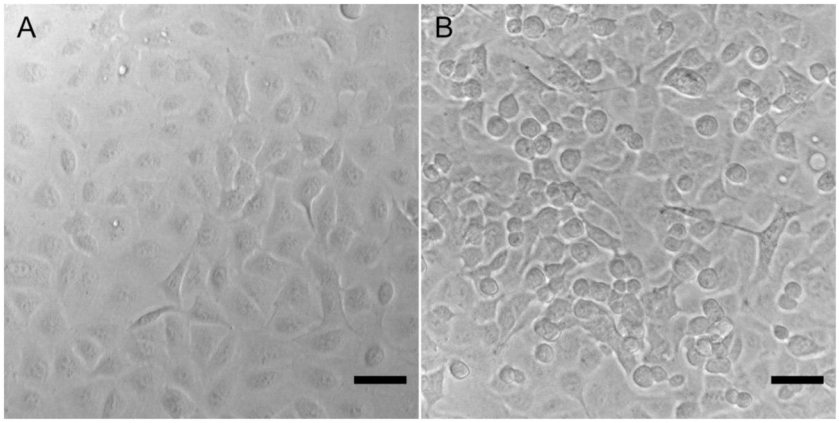

Fig. 5. Transmission images of control and PTC-209-treated A549 cells. The round-shaped non-adhering cells and the adhering cells appear at different focal planes, although the transmission detection mode can not separate them optically. Scale bars for A, B: 50 μm.

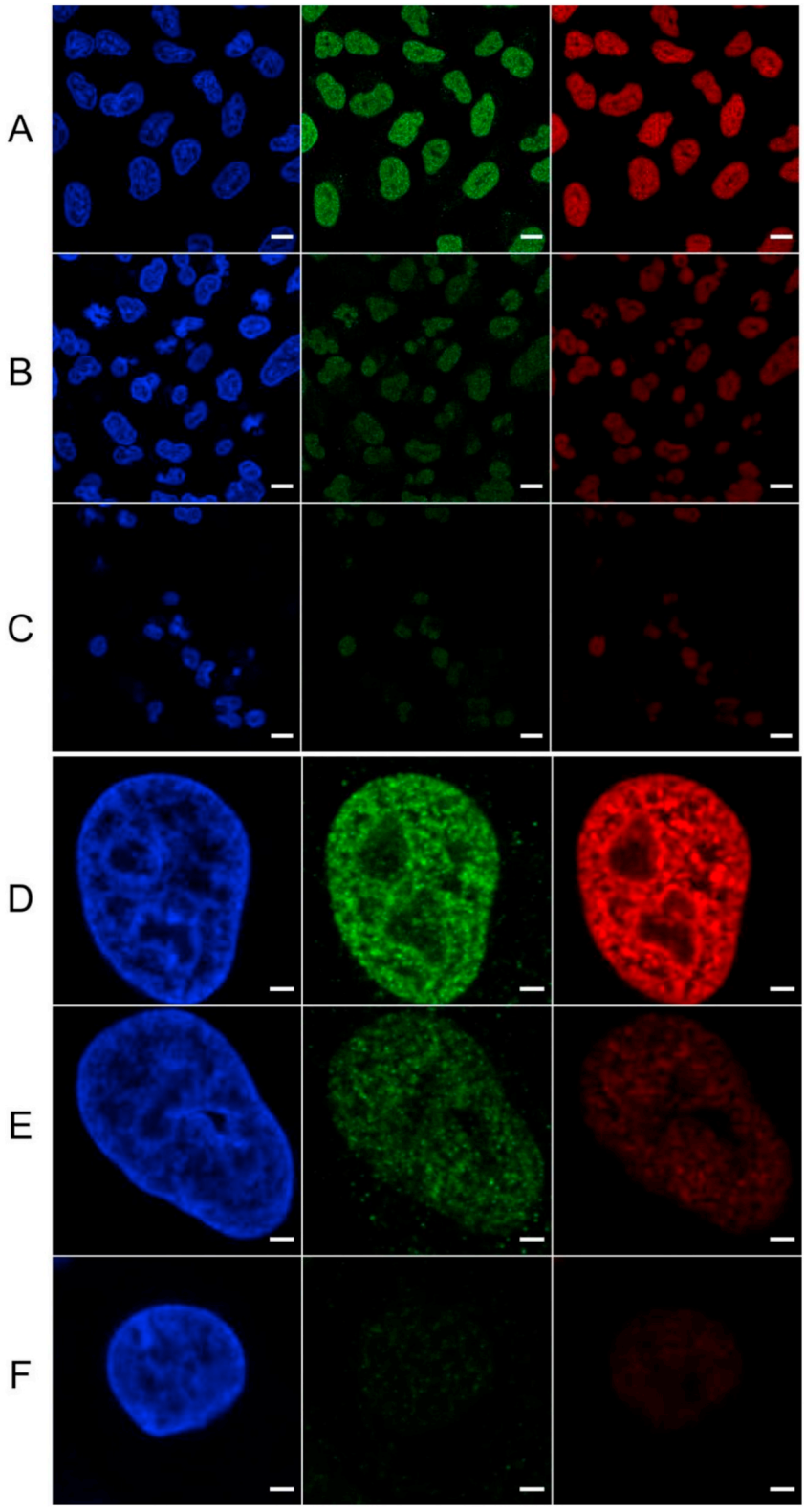

Fig. 6. Fluorescence nuclear imaging of DNA, BMI1 and uH2A in control and PTC-209-treated A549 cell line by confocal microscopy. Left panels: DNA staining by Hoechst 33342. Middle panels: BMI1 staining by immunofluorescence; secondary antibody (m-488) was labeled with Alexa488 (green acquisition channel). Right panels: uH2A staining by immunofluorescence; secondary antibody (r-647c) labeled with Alexa647 (far-red acquisition channel). Rows A,D: control cells. Rows B,E: PTC-209-treated cells, optical plane corresponding to adherent cells (z = 0 μm). Rows C,F: PTC-209-treated cells, optical plane corresponding to round-shaped non-adherent cells (z = +2.4 μm). Scale bar for A, B, C: 10 μm. Scale bar for D, E, F: 2 μm. (For interpretation of the references to colour in this figure legend, the reader is referred to the web version of this article.)

black dotted line), while the majority (~60%) shows a linear trend but with a lower slope (Fig. 7, blue dotted line). In addition, BMI1 down-regulation did not alter the nuclear area to a significant extent with respect to control (Median control: 153.5 μm^2, Median PTC-209: 157.4 μm^2, $p = .19$, Mann-Whitney Test), while instead reducing the nuclear circularity (Median control: 0.766, Median PTC-209: 0.747, $p = .002$, Mann-Whitney Test).

3.4. Colocalization analysis of BMI1 and uH2A in A549 cells

Similar to previous studies, immunofluorescence images indicated a sub-micron cluster organization of BMI1 in the nucleus (Fig. 1E). These clusters are called polycomb (PcG) bodies and they reveal chromatin regions of high density [29]. Notably, also nuclear uH2A condenses in visible sub-micron structures corresponding to domains of high H2A

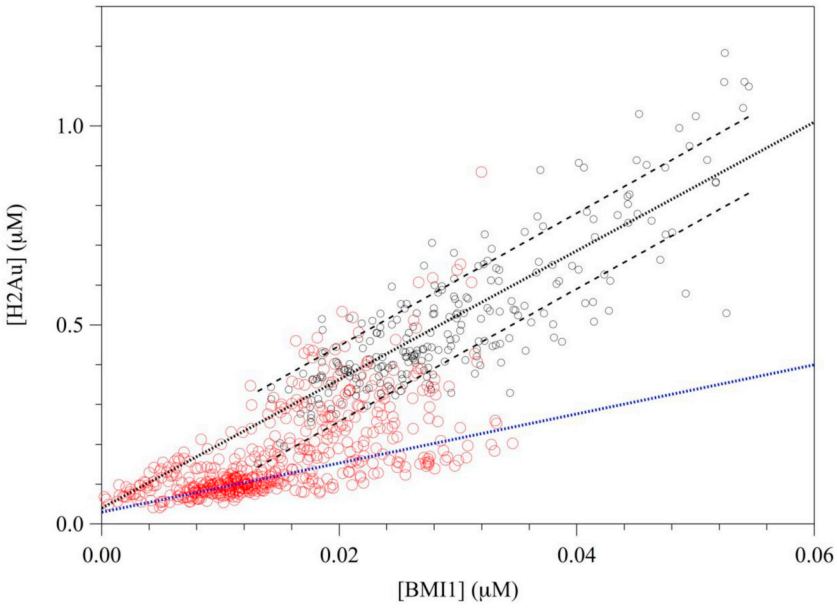

Fig. 7. uH2A *vs.* BMI1 cell plot from control and PTC-treated A549 cells. The fluorescence associated to the immunorecognition of nuclear BMI1 and uH2A is converted to protein concentrations (see Materials and Methods) and plotted. Single cell values for control and PTC-209-treated cells are reported as black and red empty circles, respectively. The black dotted line represents linear fit to control cells. 40% of treated cells are comprised between the confidence bands (black dashed lines) identified by the linear fit to control cells. 60% of treated cells fall below the lower confidence band and the blue dotted line represents linear fit to these cells. (For interpretation of the references to colour in this figure legend, the reader is referred to the web version of this article.)

ubiquitination (Fig. 1F). The cluster organization of two biomolecules in a cell is particularly suited to investigate their degree of functional co-localization, *i.e.* whether their accumulation occurs in a fixed stoichiometric ratio at a spatial scale corresponding to the resolution of the confocal microscope (240 and 270 nm for the green and far-red emission wavelengths, respectively: see Materials and Methods section). Accordingly, we calculated the Pearson's correlation coefficient R between BMI1 and uH2A on high zoomed confocal images [30]. R quantifies the degree to which the variability in BMI and uH2A pixel intensities can be explained with linear relationship between the two proteins [31]. We found a slightly positive R range (0.02–0.28). Costes' statistical test on colocalization [32], however, highlighted the poor significance ($p > .05$) of these values with respect to random spatial overlapping of the two markers. Hence, uH2A and BMI1 may indeed co-occur in the same spatial region of the nucleus, but their stoichiometric ratio is variable. This may imply that most BMI1 does not accumulate in regions where uH2A accumulates, *i.e.* that PcG bodies do not overlap (in real time) with uH2A *foci*.

3.5. Single-cell analysis of the BMI1-uH2A correlation in human tissue

The functional relationship between BMI1 and uH2A was tested also in a tissue context. IIF was carried out on a Non-Small Cell Lung Cancer (NSCLC) human biopsy analyzing both tumoral and neighboring stromal regions, identified by our pathology core. In this context, the Alexa488-labeled secondary antibody was replaced by a Cy3-labeled analog, on account of the strong autofluorescence of pulmonary tissues in the green collection channel (500–560 nm) upon 488 nm excitation. Cy3 can be excited at 561 nm and its fluorescence, which is located in the 570–610 nm range (red acquisition channel, see Materials and Methods), is weakly affected by tissue autofluorescence, and can therefore be easily decoupled from that of Alexa647. Differently than with our IIF on A549, in tissues we did not convert the collected fluorescence into antigen concentrations, because of the large optical difference between the calibration solution of the secondary antibodies and the imaged tissue.

Similarly to A549 cells, confocal images showed that BMI1 has a prominent cluster arrangement in the nuclei of cells contained within a

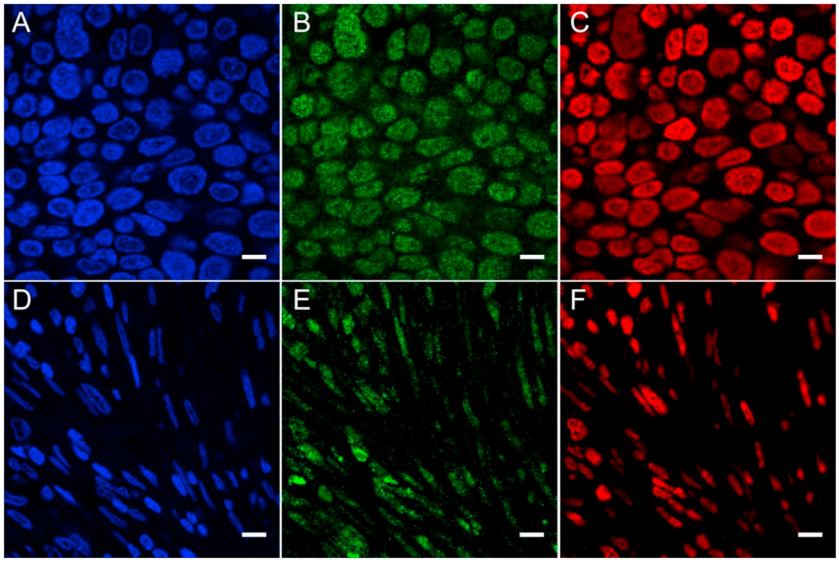

Fig. 8. Fluorescence nuclear imaging of DNA, BMI1 and uH2A in NSCLC tissue by confocal microscopy. (A-C) Tumor regions. (D-F) Stromal regions. (A, D) DNA staining by Hoechst 33342 (Blue acquisition channel). (B, E) BMI1 staining by immunofluorescence; secondary antibody (m-Cy3) labeled with Cy3 (red acquisition channel); note that fluorescence has been displayed in a green colour scale for consistency with Fig. 1B,E. (C, F) uH2A staining by immunofluorescence; secondary antibody (r-647 t) labeled with Alexa647 (far-red acquisition channel). Scale bar: 10 μm. (For interpretation of the references to colour in this figure legend, the reader is referred to the web version of this article.)

tissue structure (Fig. 8). The nuclear pattern of uH2A instead became smoother, possibly due to some resolution loss in the far-red tissue when optically heterogeneous tissue specimens are imaged.

At first, we compared the tumor with stromal regions to obtain a quantification of their morphological differences (Table 1). We found that tumor cells have more than two-fold the area of stromal cells; and that stromal cells are in general much more elongated, as quantifiable by the lower detected circularity. These features are in agreement with the recognized morphometric properties of stromal and transformed epithelial cells, and allow for their fast identification in the sample [33].

Next, we focused on the BMI and uH2A quantification in the two cellular subgroups. As expected, given its oncogenic nature, BMI1 was found to be almost two-fold more concentrated in tumor than in stromal cell nuclei (Table 1). A similar trend was noted for uH2A, although not in the same proportion as BMI1 (30% increase in neoplastic with respect to stromal regions). Remarkably, we found that BMI1 and uH2A are moderately correlated in tumor cells ($r = 0.424$, $p < .0001$), as compared to that in the A549 cell line. This moderate correlation is likely caused by the much higher cellular heterogeneity within the tumor milieu, which contains cells that are in different stages of differentiation and cell cycle progression. Such complex tissue intrinsic variability favors more variable ratios of uH2A *vs.* BMI1 concentrations, as compared to what is observed in the more homogeneous A549 cell line (Fig. 9A). An even stronger heterogeneity was observed in the tumor-associated stroma, where a fraction (< 10%) of cells was observed almost devoid of uH2A (Fig. 9B). Yet, most (90%) stromal cells mapped onto an almost linear uH2A *vs.* BMI1 trend, which is steeper compared to the neoplastic set. Overall, these findings highlight the strong biochemical relationship between uH2A and BMI1 also in NSCLC tissue context, although its features are critically dependent on the cell type.

Similarly to that observed in A549 cells, poor or no correlation ($0 < r < 0.1$) was found between nuclear area, circularity or internuclear distance and BMI1.

4. Discussion

In the last few years, a rich scientific literature highlighted the role of PCGF4, better known as BMI1, in promoting the E3-ligase activity on Lys119 of Histone 2A by the canonical Polycomb Repressor Complex 1 (cPRC1) in mammals [8,11]. Ubiquitination of H2A (uH2A) belongs to those post-translational modifications of histone proteins with a major role in the repression of gene transcription by chromatin remodeling. Accordingly, BMI1 was early identified as a protein involved in transcription regulation pathways leading to cell differentiation, senescence, and tumor [12]. In NSCLC the expression of BMI1 has a clear prognostic value [14], suggesting pivotal roles for BMI1-assisted chromatin remodeling in NSCLC.

Interestingly, this composite puzzle has been composed over the years mostly by means of classical *ex-vivo* biochemical methods. Nonetheless, the spatial and temporal features of biochemical processes *in vivo* are increasingly recognized as quintessential to understanding the mechanisms of biological regulation [17]. This knowledge has been fueled by modern microscopy techniques that allow imaging biomolecules and their interactions at spatial scales, ranging from single cells down to single molecules, and at temporal scales spanning from hours down to a few microseconds.

Adopting this perspective, we set out to answer a very basic question: can the relationship between BMI1 and uH2A at different spatial scales at the single cell level be visualized? On account of its novelty, we anticipated that the answer to such a question could help to elucidate subtle features of the BMI-promoted E3-ligase activity of cPRC1. This also prompted us to assess how BMI1 downregulation could affect the physiological relationship between BMI1 and uH2A, taking advantage of the PTC-209 compound, a strong BMI1 downregulator [14].

To this aim, we used a sensitive indirect immunofluorescence protocol conjugated to confocal fluorescence microscopy. This enabled the *quantitative* imaging of endogenous BMI1 and uH2A at the level of a single nucleus, as well as at the spatial resolution of 240–270 nm, afforded by confocal microscopy. The majority of our experiments was carried out on A549 cells, a widely used cell line adopted for NSCLC studies. The strong quantitative correlation of nuclear BMI1 and uH2A concentrations (Fig. 2) clearly indicated that the biochemical connection between the two proteins could indeed be visualized at the single nucleus level. The biochemical meaning of the strong statistical correlation between BMI1 and uH2A was benchmarked by a similar analysis on the nuclear proteins Importin-α and uH2A (Fig. 4), which do not possess any direct biochemical connection.

Notably, we observed almost linear relationships between the BMI1 and uH2A nuclear concentrations with detectable graphical intercept at zero BMI1 concentration. Two main implications arise from these results: first, since each cPRC1 complex accommodates only one BMI1 protein at any given time [34], the linear dependence can be rationalized by a direct proportionality between *the nuclear BMI1 concentration and the number* of *nuclear cPRC1 complexes*, under the reasonable hypothesis of a constant BMI1 activity in promoting the E3-ligase activity of each cPRC1. Therefore, regulation of BMI1 expression has a *linear effect* onto H2A ubiquitination and, in turn, on uH2A-assisted transcription regulation; second, the non-zero intercept may suggest that a minimal uH2A pool exists also at negligible concentrations of BMI1, possibly on account of a residual E3-ligase activity due to variant PRC1 complexes [8]. Further experiments are needed to prove such this hypothesis. However, the large uH2A amplification observed following BMI1 increase (up to fifteen-fold the average uH2A pool observed in absence of BMI1) highlights the pivotal role of BMI1 in promoting ubiquitination of H2A. Since BMI1 appears to participate only in the canonical PRC1 complex, we showed the predominant E3-ligase activity of cPRC1 with respect to variant PRC1 complexes in A549 cells. Interestingly, a very recent paper shows that this role is taken up by variant PRC1 complexes in mouse Embryonic Stem Cells (ESCs), where cPRC1 contributes little to uH2A formation [35], underlying potential differences between embryonic and adult biochemistries regarding the role of cPRC1 in defining the chromatin landscape during cellular processes such as lineage commitment, as a potential example.

Upon treatment of lung cancer cells (A549) with PTC-209 the BMI1 concentration was strongly decreased as expected, and it was followed by a concomitant decrease of uH2A, therefore providing evidence that the biochemical association between BMI1 and uH2A at nuclear level is strongly maintained. This finding correlates with the reported downregulation of Bmi1 by PTC-209 [15]. Notably, when treating A549 cells with PTC-209, in non-adhering cells (the major pool) the two markers were decreased to negligible concentrations. In the adhering cells (the minor pool), higher concentrations of BMI1 and uH2A were still detected (albeit strongly reduced with respect to control levels) (Fig. 7). About 40% of these cells followed a linear uH2A *vs* BMI1 relationship similar to that observed for untreated cells. The other 60% instead showed a linear uH2A *vs* BMI1 relationship with lower slope as compared to control. This suggests that the lower H2A ubiquitination in treated cells may be attributed to either a lower number of active cPRC1 complexes that are formed due to the reduction of BMI1 pool, or to a reduction of the E3-ligase activity of cPRC1. Overall, our results demonstrated the remarkable ability of PTC-209 to downregulate both

Table 1
Typical parameters of cell nuclei in neoplastic and stromal regions within NSCLC tissue. Average value ± standard error are reported for each parameter.

Cell type	BMI1 (a.u.)	uH2A (a.u.)	Nuclear area (μm^2)	Circularity
Tumor	7.52 ± 0.06	116 ± 1	47.5 ± 0.8	0.73 ± 0.10
Stromal	4.50 ± 0.08	90 ± 1	19.3 ± 0.3	0.66 ± 0.14

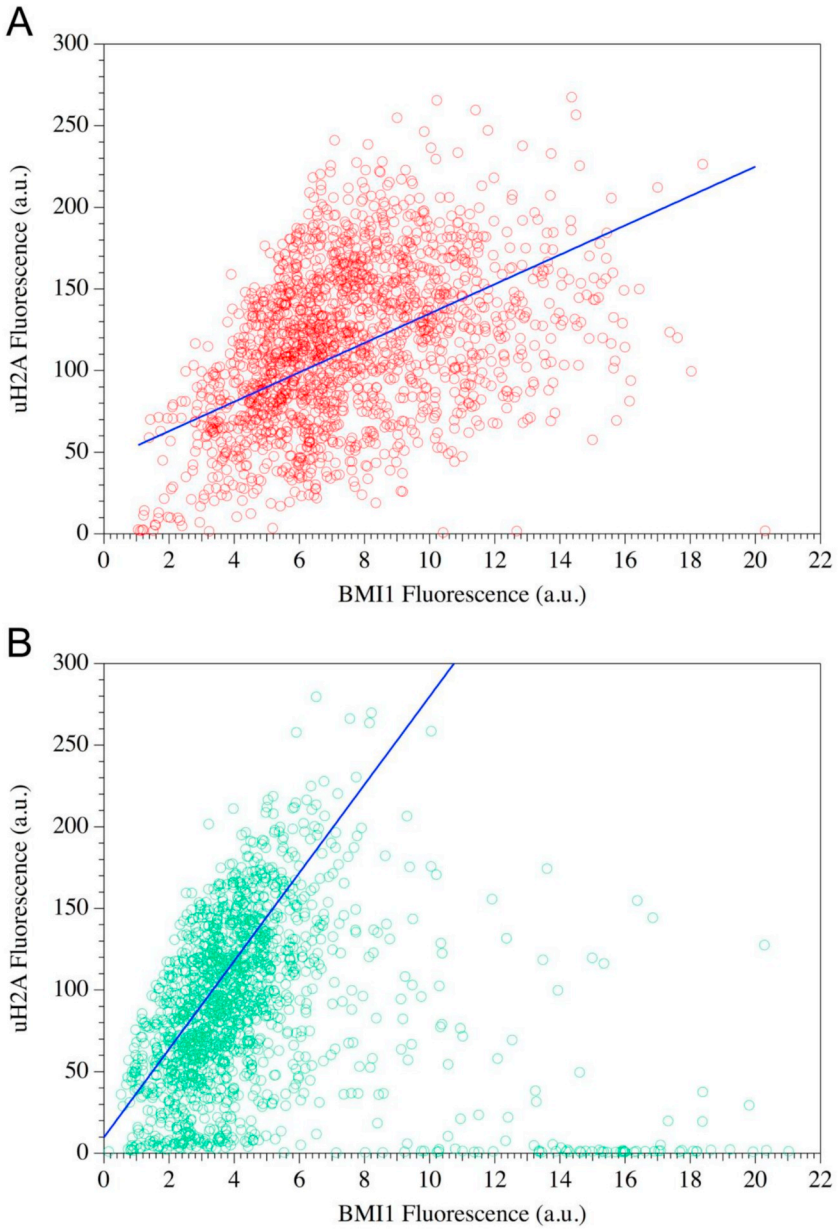

Fig. 9. uH2A *vs.* BMI1 cell plots from NSCLC tissue. (A) The fluorescence associated to uH2Au is plotted *vs.* that of BMI1 for tumor cells. (B) Same as in (A) but for stromal cells. In both cases the blue lines are the linear fitting of the data for which uH2A fluorescence is not negligible. (For interpretation of the references to colour in this figure legend, the reader is referred to the web version of this article.)

BMI1 expression and the ubiquitinating efficiency of Polycomb Complexes.

The degree of correlation between BMI1 and uH2A at the spatial resolution of 240–270 nm typical of our confocal microscope was investigated by computing the Pearson's coefficient of fluorescence co-localization *R*. Formally, a non-zero *R* with statistical significance demonstrates some degree of constant stoichiometry between the two proteins at the spatial resolution of the confocal apparatus, which in turns implies molecular interaction between the two proteins. At the confocal spatial resolution, the organization of BMI1 and uH2A into sub-micron clusters is easily discerned in our fluorescence images (Fig. 1D–F). The observed BMI1 clusters are referred to as Polycomb bodies (PcG bodies) and were identified as nuclear domains enriched in separated heterochromatin fascicles [29]. The nature of the uH2A clusters is much more elusive: they are more abundant in transformed cells and do not colocalize with other known nuclear bodies with the exception of a minor fraction of Proliferating Nuclear Cellular Antigen (PCNA)/cyclin *foci* [6]. Notably, we could not detect statistically significant positive *R* values between BMI1 and uH2A, suggesting that most BMI1 and uH2A do not assemble spatially in fixed stoichiometric ratios. This implies that the PcG bodies have a poor functional co-localization with the uH2A clusters. This puzzling scenario may be reconciled by the observed correlation of the two proteins at the whole nuclear level, by assuming a *dynamic* E3 ligase activity of BMI1-containing cPRC1. In this view, cPRC1 assembles onto the target chromatin region, ubiquitinates H2A, and then moves on to other nuclear locations to start out the process again. At each point in time, the number of active cPRC1 complexes is linearly dependent upon the BMI1 concentration, as also demonstrated upon BMI1 depletion by PTC-209. This picture adds to the recent discovery of a PcG formation mechanism and subsequent chromatin silencing that does not necessarily involve H2A ubiquitination by cPRC1. In fact, components of the polyhomeotic (Ph) protein family located within PRC1 possess a Sterile Alpha Motif (SAM) that promotes cPRC1 oligomerization onto chromatin to yield PcG

clusters of different size [36,37].

Next, we moved to visualize the functional correlation of BMI1 and uH2A in clinical NSCLC tissue, focusing our attention on tumor and neighboring stromal cell regions (Fig. 5). From a morphological point of view, epithelial tumor cells possess larger and more circular nuclei as compared to fibroblasts and other components of the stroma. Accordingly, neoplastic and stromal regions are easily recognized in the sample and can be imaged separately. On average, tumor cells were characterized by significantly higher BMI1 and uH2A concentrations (Table 1), raising the question whether the cell type has any influence on the relationship between the two proteins. Despite greater heterogeneity if compared to that in A549 cells, *in situ* tumor cells were once again characterized by a statistically significant correlation between BMI1 and uH2A at the single nuclear level. We demonstrated that the functional correlation between BMI1 and uH2A could still be visualized in a complex and highly heterogeneous stromal environment, showing that such cells split into: i) a larger pool ($> 90\%$) in which a significant protein-protein correlation was visible; and ii) a minor pool ($< 10\%$) characterized by almost no uH2A (Fig. 7). As a technical note, the variability of the tissue optical properties prevented the colocalization analysis. These findings are consistent with the highly heterogeneous nature of tumor-associated stromas, which requires more in-depth molecular investigation to comprehend how they differ and how they contribute to sustaining tumorigenicity.

Finally, for both A549 cells and tissue tumor cells we found a weak to almost null correlation between both the BMI1 and uH2A nuclear concentrations with morphological features such as nuclear area, circularity, and internuclear distance. The latter property assesses the independence of BMI1 and uH2A expression levels on the local cell density (confluence: 60–70%), therefore also highlighting the unbiased cell sampling adopted in our study. In addition, our findings suggest a weak interaction of BMI1 with the molecular factors that determine nuclear shape and size. BMI1 downregulation did not change this pattern, however it induced a statistically significant reduction in the circularity of cell nuclei.

5. Conclusions

In this work we answered positively the question whether the functional relationship between BMI1 and uH2A can be visualized in cell nuclei, at the single cell level, thereby unveiling some subtle biochemical features that are critically dependent on the spatial scale. This was accomplished by an indirect immunofluorescence protocol implemented using a confocal microscope. Experiments were carried out on both the NSCLC cell line (A549) and NSCLC tissue, on account of the recognized pivotal role of BMI1 in several types of cancer, including NSCLC.

In A549 cells we observed a linear dependence of the uH2A concentration upon BMI1 expression at the single nucleus level. This relationship is lost at submicron spatial scales comparable with those of the BMI1 and uH2A clusters that populate the nucleus. These findings have profound biochemical implications since they reveal that: 1) at the nuclear level, the association of BMI1 to cPRC1, which is needed to trigger H2A ubiquitination, occurs linearly in the physiological BMI1 concentration range; 2) in the NSCLC cell line model utilized, a minor pool of uH2A may exist in absence of BMI1, indicating non-exclusive, although predominant, role of BMI1 in the amplification of the E3-ligase activity of cPRC1; 3) Polycomb bodies and uH2A clusters display poor (if any) colocalization, suggesting a dynamic ubiquitination model of cPRC1. PTC-209, a strong downregulator of BMI1, was shown to lead to a strong reduction of both BMI1 and uH2A by combining a pure stoichiometric mechanism (lower BMI1 expression and therefore less uH2A) with a subtler reduction of global cPRC1 activity. Both pathways are fully consistent with our dynamic view of H2A ubiquitination by cPRC1.

A significant quantitative correlation between BMI1 and uH2A was found also in tissue cells, although it was slightly reduced with respect to A549 cell lines, given the tissue cellular heterogeneity (tumor *vs.* stroma), and high heterogeneity also within tumor and stroma cells. Besides highlighting the relationship between BMI1 and uH2A in different contexts, these results also validate the use of uH2A as downstream "reporter" of BMI1 activity at the nuclear level.

Starting from these results, further investigations on the temporal dynamics of BMI-promoted E3 ligase activity in living cells are ongoing.

Acknowledgments

This research, in the framework of the project "DIAMANTE - Diagnostica Molecolare Innovativa per la scelta terapeutica personalizzata dell'adenocarcinoma pancreatico" (grant number CUP I56D15000310005), was supported by the Regione Toscana Bando FAS Salute 2014 (Italy). R.B. acknowledges the funding from the Short Term Mobility 2018/2019 of the National Research Council of Italy (CNR). EL acknowledges PTC Therapeutics (South Plainfield, NJ) for donating the BMI1 pharmacological downregulator PTC-209, as well as funding from BIDMC CAO Pilot Award on Targeting BMI1 in pulmonary adenocarcinomas (USA); Yong Siew Yoon Research Grant on Strategic targeting of non-kinase pathways in NSCLC (Singapore, USA); and Progetto Bandiera MIUR on Bmi1 as a master proto-oncogene in Small and Non Small Cell Lung Cancer (Italy).

References

[1] B. Alberts, A. Johnson, J. Lewis, D. Morgan, M. Raff, K. Roberts, P. Walter, Molecular biology of the cell, Garland Science, Sixth edition, Taylor & Francis, New York, 2015.
[2] M. Lawrence, S. Daujat, R. Schneider, Lateral thinking: how histone modifications regulate gene expression, Trends Genet. 32 (2016) 42–56.
[3] J.H.A. Vissers, F. Nicassio, M. van Lohuizen, P.P. Di Fiore, E. Citterio, The many faces of ubiquitinated histone H2A: insights from the DUBs, Cell Div 3 (2008) 14.
[4] V.M. Weake, J.L. Workman, Histone ubiquitination: triggering gene activity, Mol. Cell 29 (2008) 653–663.
[5] M. Endoh, T.A. Endo, T. Endoh, K. Isono, J. Sharif, O. Ohara, T. Toyoda, T. Ito, R. Eskeland, W.A. Bickmore, M. Vidal, B.E. Bernstein, H. Koseki, Histone H2A mono-ubiquitination is a crucial step to mediate PRC1-dependent repression of developmental genes to maintain ES cell identity, PLoS Genet. 8 (2012) 2774.
[6] A.P. Vassilev, H.H. Rasmussen, E.I. Christensen, S. Nielsen, J.E. Celis, The levels of ubiquitinated histone H2A area highly up-regulated in transformed human cells -partial colocalization of uH2A clusters and PCNA/cyclin foci in a fraction of cells in S-phase, J. Cell Sci. 108 (1995) 1205–1215.
[7] C.M. Pickart, Mechanisms underlying ubiquitination, Annu. Rev. Biochem. 70 (2001) 503–533.
[8] B. Schuettengruber, H.M. Bourbon, L. Di Croce, G. Cavalli, Genome regulation by Polycomb and Trithorax: 70 years and counting, Cell 171 (2017) 34–57.
[9] L. Di Croce, K. Helin, Transcriptional regulation by Polycomb group proteins, Nat. Struct. Mol. Biol. 20 (2013) 1147–1155.
[10] Z.H. Gao, J. Zhang, R. Bonasio, F. Strino, A. Sawai, F. Parisi, Y. Kluger, D. Reinberg, PCGF homologs, CBX proteins, and RYBP define functionally distinct PRC1 family complexes, Mol. Cell 45 (2012) 344–356.
[11] A.M. Taherbhoy, O.W. Huang, A.G. Cochran, BMI1-RING1B is an autoinhibited RING E3 ubiquitin ligase, Nat. Commun. 6 (2015).
[12] R. Bhattacharya, S.B. Mustafi, M. Street, A. Dey, S.K. Dwivedi, Bmi-1: at the crossroads of physiological and pathological biology, Genes & Dis. 2 (2015) 225–239.
[13] G.P. Dimri, J.L. Martinez, J.J. Jacobs, P. Keblusek, K. Itahana, M. Van Lohuizen, J. Campisi, D.E. Wazer, V. Band, The Bmi-1 oncogene induces telomerase activity and immortalizes human mammary epithelial cells, Cancer Res. 62 (2002) 4736–4745.
[14] K.J. Yong, D.S. Basseres, R.S. Welner, W.C. Zhang, H. Yang, B. Yan, M. Alberich-Jorda, J.Y. Zhang, L.L. de Figueiredo-Pontes, C. Battelli, C.J. Hetherington, M. Ye, H. Zhang, G. Maroni, K. O'Brien, M.C. Magli, A.C. Borczuk, L. Varticovski, O. Kocher, P. Zhang, Y.C. Moon, N. Sydorenko, L.X. Cao, T.W. Davis, B.M. Thakkar, R.A. Soo, A. Iwama, B. Lim, B. Halmos, D. Neuberg, D.G. Tenen, E. Levantini, Targeted BMI1 inhibition impairs tumor growth in lung adenocarcinomas with low CEBP alpha expression, Sci. Transl. Med. 8 (2016).
[15] Q. Wang, Z.W. Li, Y.P. Wu, R. Huang, Y.M. Zhu, W. Zhang, Y.L. Wang, J. Cheng, Pharmacological inhibition of Bmi1 by PTC-209 impaired tumor growth in head neck squamous cell carcinoma, Cancer Cell Int. 17 (2017) 14.
[16] L.X. Cao, J. Bombard, K. Cintron, J. Sheedy, M.L. Weetall, T.W. Davis, BMI1 as a novel target for drug discovery in Cancer, J. Cell. Biochem. 112 (2011) 2729–2741.
[17] J.D. Scott, T. Pawson, Cell signaling in space and time: where proteins come together and when They're apart, Sci. 326 (2009) 1220–1224.
[18] A.S. Stender, K. Marchuk, C. Liu, S. Sander, M.W. Meyer, E.A. Smith, B. Neupane,

G.F. Wang, J.J. Li, J.X. Cheng, B. Huang, N. Fang, Single cell optical imaging and spectroscopy, Chem. Rev. 113 (2013) 2469–2527.
[19] G. Abbandonato, B. Storti, G. Signore, F. Beltram, R. Bizzarri, Quantitative optical lock-in detection for quantitative imaging of switchable and non-switchable components, Microsc. Res. Tech. 79 (2016) 929–937.
[20] B. Storti, E. Margheritis, G. Abbandonato, G. Domenichini, J. Dreier, I. Testa, G. Garau, R. Nifosi, R. Bizzarri, Role of Gln222 in Photoswitching of Aequorea fluorescent proteins: a twisting and H-bonding affair? ACS Chem. Biol. 13 (2018) 2082–2093.
[21] S. Rodenhuis, R.J.C. Slebos, Clinical significance of RAS oncogene activation in human lung cancer, Cancer Res. 52 (1992) S2665–S2669.
[22] L.K. Huang, M.J.J. Wang, Image thresholding by minimizing the measures of fuzziness, Pattern Recogn. 28 (1995) 41–51.
[23] G. Tortarolo, M. Castello, A. Diaspro, S. Koho, G. Vicidomini, Evaluating image resolution in stimulated emission depletion microscopy, Optica 5 (2018) 32–35.
[24] P. Bianchini, F. Cardarelli, M. Di Luca, A. Diaspro, R. Bizzarri, Nanoscale protein diffusion by STED-based pair correlation analysis, PLoS One 9 (2014) e99619.
[25] S.V. Costes, D. Daelemans, E.H. Cho, Z. Dobbin, G. Pavlakis, S. Lockett, Automatic and quantitative measurement of protein-protein colocalization in live cells, Biophys. J. 86 (2004) 3993–4003.
[26] J.W. Voncken, D. Schweizer, L. Aagaard, L. Sattler, M.F. Jantsch, M. van Lohuizen, Chromatin-association of the Polycomb group protein BMI1 is cell cycle-regulated and correlates with its phosphorylation status, J. Cell Sci. 112 (1999) 4627–4639.
[27] A.Z. Khan, T.P. Utheim, C.J. Jackson, S. Reppe, T. Lyberg, J.R. Eidet, Nucleus morphometry in cultured epithelial cells correlates with phenotype, Microsc. Microanal. 22 (2016) 612–620.
[28] L.F. Yang, Y.J. Xing, J.X. Xiao, J. Xie, W. Gao, J.Q. Xie, L.T. Wang, J.H. Wang, M.Y. Liu, Z.F. Yi, W.W. Qiu, Synthesis of Cyanoenone-modified Diterpenoid analogs as novel Bmi-1-mediated antitumor agents, ACS Med. Chem. Lett. 9 (2018) 1105–1110.
[29] J. Smigova, P. Juda, D. Cmarko, I. Raska, Fine structure of the "PcG body" in human U-2 OS cells established by correlative light-electron microscopy, Nucleus-Austin 2 (2011) 219–228.
[30] V. Zinchuk, O. Zinchuk, T. Okada, Quantitative colocalization analysis of multicolor confocal immunofluorescence microscopy images: pushing pixels to explore biological phenomena, Acta Histochem. Cytochem. 40 (2007) 101–111.
[31] K.W. Dunn, M.M. Kamocka, J.H. McDonald, A practical guide to evaluating colocalization in biological microscopy, Am. J. Physiol.-Cell Physiol. 300 (2011) C723–C742.
[32] J. Adler, I. Parmryd, Quantifying Colocalization by correlation: the Pearson correlation coefficient is superior to the Mander's overlap coefficient, Cytom Part A 77A (2010) 733–742.
[33] B. Lahrmann, N. Halama, H.P. Sinn, P. Schirmacher, D. Jaeger, N. Grabe, Automatic tumor-stroma separation in fluorescence TMAs enables the quantitative high-throughput analysis of multiple Cancer biomarkers, PLoS One 6 (2011) 11.
[34] J. Gil, A. O'Loghlen, PRC1 complex diversity: where is it taking us? Trends Cell Biol. 24 (2014) 632–641.
[35] N.A. Fursova, N.P. Blackledge, M. Nakayama, S. Ito, Y. Koseki, A.M. Farcas, H.W. King, H. Koseki, R.J. Klose, Synergy between variant PRC1 complexes defines Polycomb-mediated gene repression, Mol. Cell 74 (2019) 1020.
[36] K. Isono, T.A. Endo, M.C. Ku, D. Yamada, R. Suzuki, J. Sharif, T. Ishikura, T. Toyoda, B.E. Bernstein, H. Koseki, SAM domain polymerization links subnuclear clustering of PRC1 to gene silencing, Dev. Cell 26 (2013) 565–577.
[37] A.H. Wani, A.N. Boettiger, P. Schorderet, A. Ergun, C. Munger, R.I. Sadreyev, X. Zhuang, R.E. Kingston, N.J. Francis, Chromatin topology is coupled to Polycomb group protein subnuclear organization, Nat. Commun. 7 (2016).